Materials Science & Engineering A 874 (2023) 145007

Contents lists available at ScienceDirect

Materials Science & Engineering A

journal homepage: www.elsevier.com/locate/msea

A lightweight Fe–Mn–Al–C austenitic steel with ultra-high strength and ductility fabricated via laser powder bed fusion

Raiyan Seede [a,b], Austin Whitt [a], Jiahui Ye [c], Sean Gibbons [d], Philip Flater [e], Bernard Gaskey [e], Alaa Elwany [c], Raymundo Arroyave [a,c], Ibrahim Karaman [a,*]

[a] Department of Materials Science and Engineering, Texas A&M University, College Station, 77843, TX, USA
[b] Materials Science Division, Lawrence Livermore National Laboratory, Livermore, 94550, CA, USA
[c] Wm Michael Barns '64 Department of Industrial and Systems Engineering, Texas A&M University, College Station, 77843, TX, USA
[d] Operations Division, AFWERX, Eglin Air Force Base, 32542, FL, USA
[e] Fuze & Warhead Research Branch, Air Force Research Laboratory, Eglin Air Force Base, 32542, FL, USA

ARTICLE INFO

Keywords:
Laser powder bed fusion
Additive manufacturing
Selective laser melting
Lightweight steel
High strength steel

ABSTRACT

Lightweight Fe–Mn–Al–C steels have become a topic of significant interest for the defense and automotive industries. These alloys can maintain high strength and ductility while also reducing weight in structural applications. Conventionally processed Fe–Mn–Al–C austenitic steels with high Al content (~9 wt%) demonstrate greater than 1.5 GPa strength with 35% elongation. Several recent studies have demonstrated success in fabricating steel parts using laser powder bed fusion (L-PBF) additive manufacturing (AM), which can generate near-net-shape components with complex geometries and is capable of local microstructural control. However, studies on L-PBF processing of Fe–Mn–Al–C alloys have focused on low Al content (<5 wt%) compositional regimes representing alloys that undergo transformation-induced plasticity (TRIP) and twinning-induced plasticity (TWIP). Here, we present the effects of L-PBF processing on the microstructure and mechanical properties of an Fe–30Mn–9Al–1Si-0.5Mo-0.9C austenitic steel. A process optimization framework is employed to determine an ideal L-PBF processing space that will result in >99% density parts. Implementing this framework resulted in near-fully dense specimens fabricated over a broad range of process parameters. Additionally, two bi-directional scan rotation strategies (90° and 67°) were applied to understand their effects on texture and anisotropy in this material. As-printed specimens displayed considerable work-hardening characteristics with average strengths of up to 1.3 GPa and 36% elongation in the build direction. However, solidification microcracks oriented in the build direction resulted in anisotropy in tensile strength and ductility resulting in average strengths of 1.1 GPa and 20% elongation perpendicular to the build direction. The successful L-PBF fabrication of Fe–30Mn–9Al–1Si-0.5Mo-0.9C presented here is expected to open new avenues for weight reduction in structural applications with a high degree of control over part topology.

1. Introduction

The additive manufacturing (AM) method laser powder bed fusion (L-PBF) can generate parts with complex geometries that are difficult or impossible to replicate with traditional processing techniques. Many alloy systems have been successfully fabricated with L-PBF, including austenitic and martensitic steels [1–4], nickel-based super alloys [2,5–8], Al–Si–Mg alloys [2,9,10], Ti–6Al–4V [2,11,12], and numerous other alloy systems [13–16].

Fe–Mn–Al–C alloys have been the subject of recent interest for AM due to their high specific strength and toughness for weight critical applications. Several studies have focused on Fe–Mn–Al–C alloys that display twinning-induced plasticity (TWIP) and transformation-induced plasticity (TRIP), which typically contain less than 5 wt% aluminum [17–20]. These alloys have been successfully fabricated via L-PBF with excellent strength and ductility in the as-printed condition. Köhnen et al. [17] utilized L-PBF to fabricate Fe–21Mn-(X)Al-0.3C with various Al contents (X = 0–5 wt%). They reported an ultimate tensile strength of greater than 800 MPa and 30% elongation in specimens tested perpendicular to the building direction at 5 wt% Al content. Anisotropy was

* Corresponding author.
E-mail address: ikaraman@tamu.edu (I. Karaman).

https://doi.org/10.1016/j.msea.2023.145007
Received 28 February 2023; Received in revised form 1 April 2023; Accepted 3 April 2023
Available online 6 April 2023

observed in the mechanical properties of this alloy, with a ~75 MPa drop in UTS observed along the building direction. Li et al. [19] reported an UTS of 1625 MPa and 7.8% elongation in an Fe–10Mn-1.6Al-0.4C-0.7V alloy fabricated via L-PBF.

While the mechanical properties of TRIP and TWIP steels are impressive, the low Al content of these alloy systems constrains their weight reduction potential. Aluminum additions stabilize body-centered-cubic (BCC) ferrite in steels and suppress TWIP and TRIP effects, promoting dislocation glide instead [21,22]. However, the addition of Al in Fe–Mn–Al–C alloys increases their solidification range, making them prone to solidification cracking and cavitation [21]. Austenitic Fe–Mn–Al–C steels have been demonstrated to achieve excellent mechanical properties due to the precipitation hardening effect of κ-carbide precipitates [21,23–26]. To stabilize face-centered-cubic (FCC) austenite in a steel with significant Al additions, relatively high Mn contents (20–30 wt%) are required [27]. This can render higher Al content Fe–Mn–Al–C challenging to fabricate with L-PBF. Defects such as solidification cracking may be possible to mitigate by optimizing L-PBF process parameters [28,29]. Seede et al. [3] recently proposed a process parameter optimization framework to develop optimal process windows for new alloys utilizing information gathered from single track scans. This framework has been validated for various alloy systems including Ni-based alloys, steels, and shape memory alloys [3,30–34]. Development of these process windows may allow for printing defect-free parts of Fe–Mn–Al–C with higher Al content.

The lightweight and high strength Fe–30Mn–9Al–1Si-0.5Mo-0.9C alloy is of significant interest for automotive and defense applications due to its excellent mechanical properties and weight reduction potential [21,27]. This austenitic alloy offers up to 17% weight reduction compared to traditional Cr–Mo steels with comparable strength and fracture toughness [27]. Traditionally processed Fe–30Mn–9Al–1Si-0.5Mo-0.9C displays ultimate tensile strengths of up to 1.5 GPa with ~35% tensile elongation [35]. However, recent investigations have shown that traditionally processed Fe–30Mn–9Al–1Si-0.5Mo-0.9C has significant anisotropy in mechanical properties, in particular in tensile ductility, due to the formation of large, laminated Mn segregation structures that result in extreme anisotropy in ductility under tensile loading [35]. Additive processing techniques such as L-PBF have been shown to refine microstructural features which may result in a reduction in mechanical anisotropy in Fe–30Mn–9Al–1Si-0.5Mo-0.9C. Additionally, fabrication of geometrically complex components with these properties is of great value for industrial applications. The large solidification ranges of Mn- and Al-rich Fe–Mn–Al–C steel renders L-PBF fabrication without solidification cracks difficult, and there is currently no known literature on fabricating Fe–30Mn–9Al–1Si-0.5Mo-0.9C or any other Al-rich austenitic Fe–Mn–Al–C steel using L-PBF AM. This work presents a systematic study on the effect of process parameters on microstructure and mechanical properties in Fe–30Mn–9Al–1Si-0.5Mo-0.9C. A process optimization strategy developed in Ref. [3] to achieve full part density is implemented to investigate the range of process parameters which result in optimal part density for Fe–30Mn–9Al–1Si-0.5Mo-0.9C. Near-fully dense parts are then fabricated across a range of parameters to assess their role on microstructural evolution and mechanical properties in Fe–30Mn–9Al–1Si-0.5Mo-0.9C.

2. Experimental methodology

2.1. Process parameter optimization

To establish an optimum window in the laser power-velocity parameter space that mitigates porosity in Fe–30Mn–9Al–1Si-0.5Mo-0.9C, an optimization framework described in Ref. [3] is employed. An analytical thermal model developed by Eagar and Tsai (E-T) [36] is utilized to provide computationally inexpensive predictions of melt pool dimensions such as melt pool width (W) and depth (D) across the parameter space. The laser power-velocity parameter space is then sampled with single tracks to perform statistical calibration for improved model prediction accuracy. Markers in Fig. 1 display laser power-velocity combinations selected using grid-based sampling at sixty-one locations in the parameter space. Laser power (P) and scan speed (v) boundaries were chosen to be (P_{min}, P_{max}) = {35, 260 W} and (v_{min}, v_{max}) = {0.05, 2.5 m/s}. Machine limitations were used to bound P_{max} and v_{max}, and v_{min} was chosen to avoid sluggish scan velocities. P_{min} corresponds to E-T model predictions of the lowest power capable of achieving a melt pool depth of at least one layer thickness (t) at v_{min}. Two regions of the $P - v$ space were sampled. Forty parameter sets were selected between v_{min} = 0.05 m/s – v = 1.3 m/s, and 21 were selected between v = 1.3 m/s – v_{max} = 2.5 m/s. Lower scan speed values were more densely sampled as they are expected to result in more successful parts. Defect modes such as keyholing and balling were classified qualitatively in single tracks based on top-view and cross sectional micrographs and characteristic melt pool features which are well established in the literature [2,3,37–39]. Melt pool depth ≤ layer thickness ($D \leq t$) was used as a criterion from the literature to classify lack of fusion in single tracks [3,30,37].

Kennedy and O'Hagan [40] developed a statistical calibration methodology that is implemented to improve the prediction accuracy of the E-T model. A surrogate model is constructed using Gaussian process regression and measured melt pool dimensions are utilized for calibration. A discrepancy function is then used to further improve the accuracy of the calibrated model. The fully calibrated model then outputs melt pool dimension predictions across the laser power-scan speed parameter space. These predictions, as well as melt pool dimension relationships established in the literature, are used to identify the lack of fusion and keyholing regions of the processing space displayed in Fig. 1. A relationship between melt pool width and depth (namely: W/D) is used to identify the keyholing defect region and melt pool depth/layer thickness (D/t) is used to establish a lack of fusion region [3,37,41–43]. Experimentally classified keyhole single tracks are compared with several keyhole criteria in Fig. 1 to determine which criterion most accurately identifies the defect region. These criteria are selected based on established literature values ($W/D \leq$ 1.2, 1.5, 2.0) [3]. The keyholing criterion W/D ≤ 1.2 was observed to fit the experimental observations best for Fe–30Mn–9Al–1Si-0.5Mo-0.9C. As with classification in single tracks, the criterion used to establish the lack of fusion defect region was selected as $D/t \leq 1$. A 3rd degree polynomial kernel support vector machine (SVM) classifier [44,45] was used to split the processing space into balling and non-balling regions based on experimental single track classifications. A finalized process map for Fe–30Mn–9Al–1Si-0.5Mo-0.9C can be established by plotting each of these defect criteria. It should be noted that since there may be machine to machine differences in single track morphology, the methodology implemented here is intended to be machine specific.

Single track melt pool morphology is also employed to select hatch spacing values that result in full density parts using a geometrical hatch spacing criterion [3]. This criterion was derived with two major assumptions, namely, that above and below the printing surface a parabolic cross-sectional melt pool morphology exists and that layer thickness and melt pool height are equivalent. This results in the derivation of a maximum hatch spacing (h_{max}) value that will ensure the mitigation of lack of fusion porosity between laser scans:

$$h_{max} = W\sqrt{1 - \frac{t}{(t + D)}} \quad (1)$$

where W is the melt pool width, D is the melt pool depth, and t is the selected layer thickness which is held constant in this study. This equation determines a boundary for h_{max} at any location in the $P - v$ space as simply a function of single track dimensions and layer thickness, with the melt pool dimensions predicted using the calibrated,

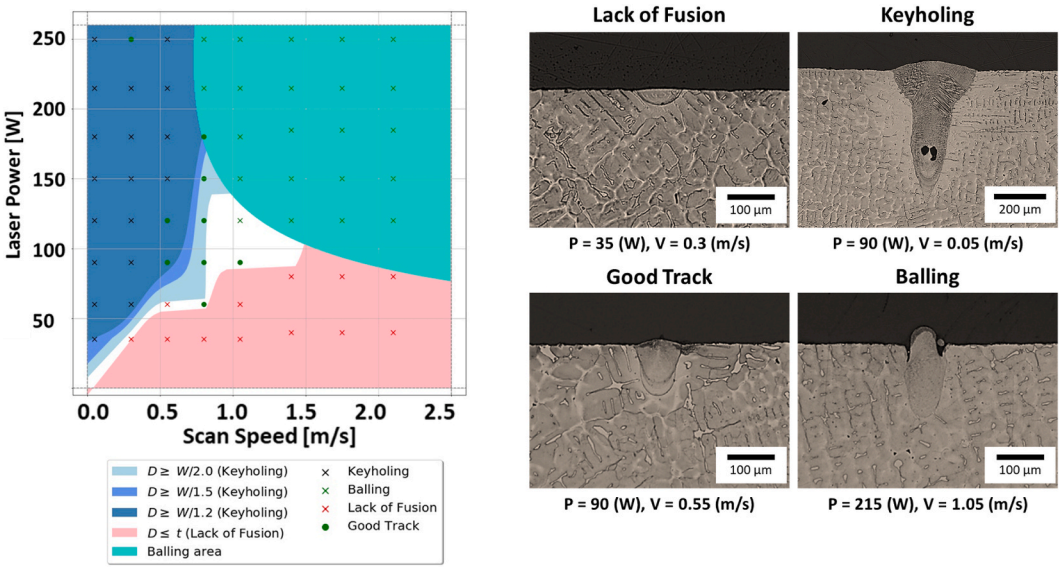

Fig. 1. A L-PBF $P - v$ map is displayed for Fe–30Mn–9Al–1Si-0.5Mo-0.9C. The map contains several keyholing criteria ($W/D \leq 1.2, 1.5, 2.0$) to ascertain the optimal criterion, and a lack of fusion criterion ($D \leq$ t). A Support Vector Machine (SVM) classifier used to identify the parameter space where balling was observed is also plotted. Experimental observations of single tracks with keyholing, lack of fusion, balling, and good track characteristics are displayed as markers in the process map, and optical micrographs showing the characteristic morphology of these tracks are displayed to the right of the process map. *W*: Melt Pool Width, *D*: Melt Pool Depth, *t*: Powder Layer Thickness.

surrogate E-T model. Maximum hatch spacing contours are plotted in a finalized process map in Fig. 2 for Fe–30Mn–9Al–1Si-0.5Mo-0.9C. Three different $P - v - h$ parameter sets listed in Table 1 were selected to fabricate 8 × 8 × 8 mm specimens guided by the processing maps in Fig. 2 within the optimal processing window. Hatch spacing values were rounded down to the nearest multiple of 5 µm for each of the parameter sets. Cubes were printed with a bi-directional scan strategy and two different scan rotation angles, namely, 90° and 67° to determine the effect of scan rotation on microstructure and mechanical properties in Fe–30Mn–9Al–1Si-0.5Mo-0.9C.

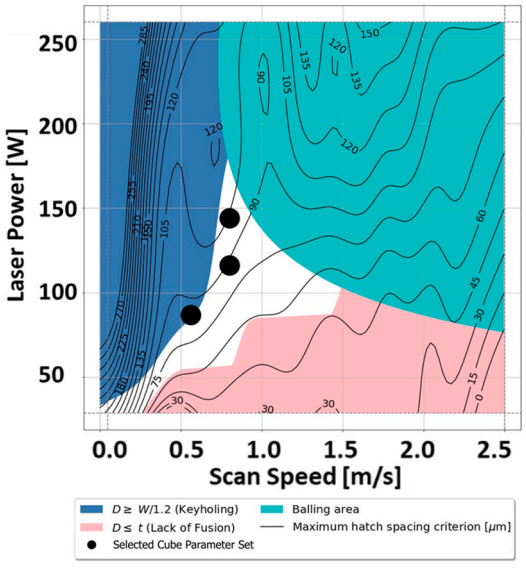

Fig. 2. A finalized L-PBF process parameter map for Fe–30Mn–9Al–1Si-0.5Mo-0.9C with keyholing, lack of fusion, and balling criteria overlayed with maximum hatch spacing contours. $W/D \leq 1.2$ is selected to represent the keyholing region. Lack of fusion is represented with a criterion of $D \leq t$, and a SVM classifier was used to fit experimental observations of balling. *W*: Melt Pool Width, *D*: Melt Pool Depth, *t*: Powder Layer Thickness.

2.2. Materials fabrication and characterization

Fe–30Mn–9Al–1Si-0.5Mo-0.9C powder was gas atomized and procured from Nanoval GmbH & Co. KG with a cumulative size distribution at 50% (i.e. D50) and 80% (i.e. D80) of 21.4 µm and 35 µm respectively. The nominal composition of Fe–30Mn–9Al–1Si-0.5Mo-0.9C as well as the composition of the powder measured by inductively coupled plasma atomic emission spectroscopy (ICP-AES) is listed in Table 2.

A 3D systems ProX DMP 200 L-PBF machine containing a Gaussian profile fiber laser, wavelength of $\lambda = 1070$ nm, and a beam diameter of 80 µm was used to print all specimens in this work. Parts were printed under a high purity argon atmosphere for protection against oxygen contamination. An as-cast base plate with the same nominal composition as the powder was used for printing single tracks. Sixty-one single tracks were printed 10 mm in length with 1 mm spacing between each track. The parameters selected for single tracks and representative micrographs of different melt pool morphologies are displayed in Fig. 1. These tracks were printed with a powder layer thickness of 35 µm corresponding to the 80th percentile of the powder size distribution. Electrical discharge machining (EDM) was utilized to cut cross sections of the single tracks, and these cross sections were polished to 0.25 µm with a water-based diamond suspension and vibratory polished in 0.04 µm colloidal silica for 2 h. A 4% Nital solution (4 ml HNO_3, 96 ml ethanol) was used to etch the single tracks to reveal melt pool morphology. The widths and depths of three cross sections were measured for each single track using optical microscopy and averaged to obtain representative melt pool dimension values.

Square 8 × 8 × 8 mm cubes were printed based on the process optimization strategy discussed in Section 2.1, and the parameters used to print each cube are listed in Table 1. The density of the as-printed cubes was measured using the Archimedes method (ASTM B962-15). All as-printed cubes were measured to have an Archimedes density of greater than 99%. EDM was used to cut cross sections of each cube, and the same polishing procedure was implemented to prepare the cubes for microstructural analysis as was described for single tracks. Three optical micrographs were taken from each of the polished cross sections and the software ImageJ® [46] was used to determine the area fraction of porosity in each of the cubes. Porosity values determined by image analysis were averaged from the measurements conducted in each of the

Table 1
A list of the parameters selected to fabricate 8 × 8 × 8 mm specimens in the optimal window of the process map in Fig. 2.

Cube	Laser Power (W)	Scan Speed (m/s)	Hatch Spacing (μm)	Scan Rotation (°)	Layer Thickness (μm)	Substrate Temperature (°C)
1	90	0.55	90	90	35	25
2	120	0.80	85	90		
3	150	0.80	105	90		
4	90	0.55	90	67		
5	120	0.80	85	67		
6	150	0.80	105	67		

Table 2
Fe–30Mn–9Al–1Si-0.5Mo-0.9C austenitic steel nominal composition and powder composition measured by Inductively Coupled Plasma – Atomic Emission Spectroscopy (ICP-AES) and combustion infrared absorbance.

Elements (wt.%)	Nominal	Powder
Fe[a]	58.5	57.12
Mn	30	32.21
Al	9	8.17
Si	1	1.05
Mo	0.5	0.49
C[b]	0.9	0.9
S	<0.01	0.007
P	<0.005	0.021

[a] Determined by difference.
[b] Determined by combustion-infrared absorbance.

three optical micrographs for each cube.

Optical micrographs of single tracks and cubes were obtained using a Keyence VH-X digital microscope with a VH-Z100 wide range zoom lens. Backscatter electron micrographs were obtained using a FEI Quanta 600 Field Emission scanning electron microscope (SEM). Quantitative composition maps were acquired using wavelength dispersive spectroscopy (WDS) on a LaB_6 equipped CAMECA SXFive electron probe microanalyzer. Parameters used to collect WDS data were 15 kV, 50 nA, 110 μs pixel dwell time, and a step size of 0.1 μm. X-ray diffraction (XRD) patterns were collected with a Bruker D8 Discover X-ray Diffractometer with a Vantec 500 area detector and a Cu K-α source. A scan rate of 1.5° per minute, a step size of 0.01°, and a maximum power of 40 kV were used to acquire XRD patterns. XRD was conducted normal to the building direction in all as-printed specimens. A Thermo Scientific Helios G4 DualBeam FIB/SEM equipped with an EDAX Team® detector was used to collect electron backscattered diffraction (EBSD) maps at 250x magnification, 20 kV, and 400 nm step size. EBSD maps were minimally post-processed in EDAX's Orientation Imaging Microscopy (OIM) software. All EBSD maps were taken from the center of the as-printed Fe–30Mn–9Al–1Si-0.5Mo-0.9C cube cross sections.

Flat dog bone tension specimens were EDM cut from as-printed rectangular 10 × 10 × 30 mm prisms fabricated with the same parameters as the cubes listed in Table 1. These rectangular prisms were printed both parallel and perpendicular to the building direction to characterize anisotropy in the mechanical properties. The tension specimens were cut with 26 mm overall length and 8 × 3 × 1 mm gauge dimensions. Tension testing was conducted with an MTS 810 servohydraulic test frame at room temperature. Three tension tests were conducted for each parameter set at an effective strain rate of 5×10^{-4} s^{-1}, and the three tests were averaged to determine the tabulated mechanical

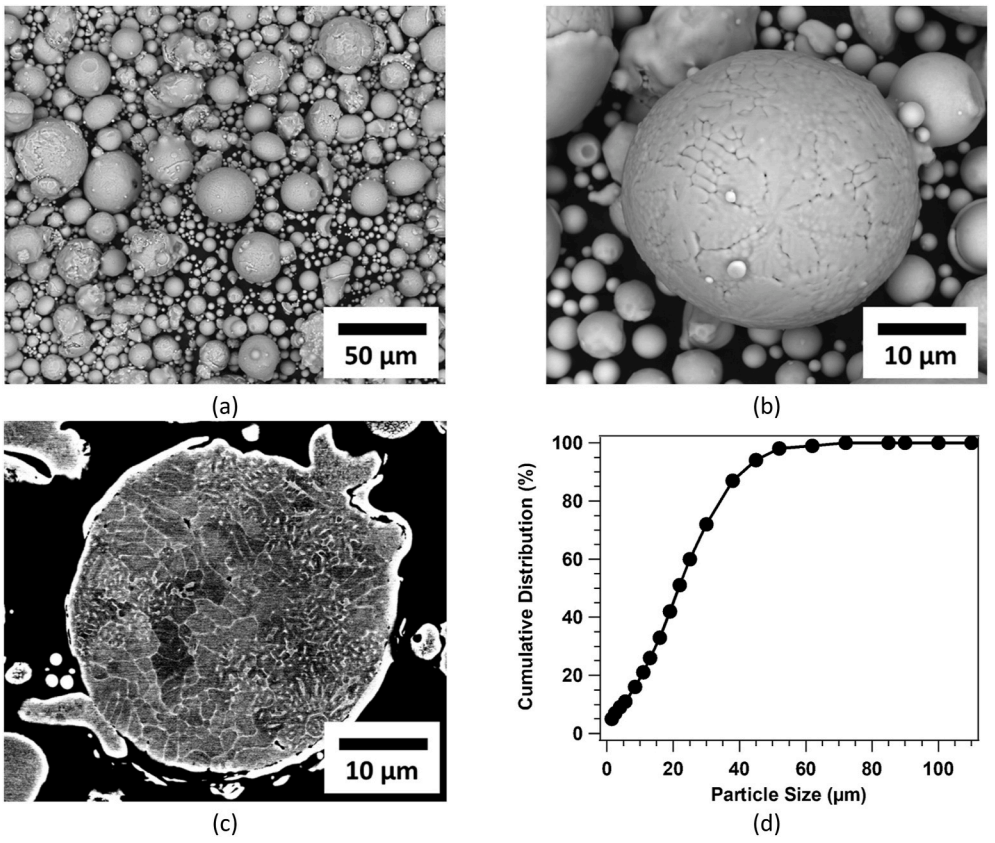

Fig. 3. Backscattered electron micrographs of gas atomized powder. a) A micrograph taken at low magnification displaying the powder distribution and morphology. High magnification micrographs b) displaying the surface morphology of an individual particle and the cross section of a particle. c) Grains and cellular segregation structures are observable in the powder cross section. d) A cumulative powder size distribution graph showing the powder sizes ranged from 0 to 60 μm, and the D50 of the powder is 21.4 μm.

property values reported in this study.

3. Results and discussion

3.1. Powder characterization

Fe–30Mn–9Al–1Si-0.5Mo-0.9C powder surface morphology, internal microstructure, and powder size distribution are displayed in Fig. 3. The particles are mostly spherical with some satellite particles observed on the surfaces of larger particles. Microdendritic features are identifiable on the surface of the powder as can be seen in Fig. 3b. In powder cross sections (Fig. 3c) cellular dendritic structures are also observable. Elemental segregation of Mn is typically observed in as-cast and L-PBF steels with high Mn content [18,20,47,48]. The cellular dendritic structures in the powder in Fig. 3c likely contain increased amounts of Mn due to the large solidification range of this alloy and the proclivity of Mn to segregate during solidification.

3.2. Density and microstructure

Optical micrographs showing the residual porosity in as-printed Fe–30Mn–9Al–1Si-0.5Mo-0.9C cubes are displayed in Fig. 4. As discussed in Section 2.2, each of the cubes printed in this study were measured to have greater than 99% Archimedes density. Image analysis revealed that each of the cube cross sections contains less than 0.50% porosity, and all but one of the cubes was measured to have less than 0.30% porosity. The lowest porosity was measured in cube 1 at 0.20%. Additionally, the cubes printed with a scan rotation of 90° (cubes 1–3) were observed to contain lower amounts of porosity compared to those printed with a 67° scan rotation (cubes 4–6). However, since image thresholding only considers pixel intensities when calculating the porosity values, higher magnification microstructural analysis is necessary to determine whether these results are indicative of differences in porosity within the cubes.

Low magnification backscattered electron micrographs displayed in Fig. 5 reveal spherical porosity and microcracks within the as-fabricated cubes. These small (<20 μm) spherical pores are typically detected in parts fabricated with gas atomized powder [2], and were observed in all of the cubes printed in this study. Differences in the amount of microcracks were observed in each of the cubes. Cracking was most prevalent in cube 6, where microcracks of up to 65 μm in length were observed. Shorter and fewer microcracks were observed in cubes 1–5, with crack lengths generally ranged from 5 to 50 μm. These results indicate that it is differences in microcracking, not porosity, that cause the discrepancy in image thresholded porosity values reported in Fig. 4. Columnar grains are observed to be oriented in the build direction in all specimens. Additionally, the majority of microcracks are observed to be oriented in the build direction along grain boundaries in each of the cubes.

Melt pool structures indicated by white dotted lines are observed in high magnification backscattered electron micrographs displayed in Fig. 6a – c. Austenitic grains oriented in the build direction are uninterrupted by melt pool boundaries, some of which are observed to extend over multiple layers. This indicates epitaxial grain growth as has been reported in the literature for Fe–Mn–Al–C and other alloys processed by L-PBF [2,17,18]. During laser melting, previous layers of material are partially remelted, and grains grow epitaxially from pre-existing grains during solidification. The need for nucleating new grains is therefore eliminated as epitaxial grain growth has a lower activation energy barrier. Resultant columnar grains are typically oriented in the build direction with a preferred crystallographic growth direction of <1 0 0> in FCC alloys which can cause anisotropic mechanical properties.

Cellular and columnar microdendritic sub-grain structures are observable in Fig. 6e – f. These features have been reported to contain Mn and C segregation in L-PBF fabricated TRIP and TWIP high manganese steels [17,18]. Wavelength dispersive spectroscopy compositional analysis displayed in Fig. 7 shows light segregation of Mn and Si in these cellular dendritic regions within the melt pools. More prominent segregation of Mn and Si is observed along melt pool boundaries. Al appears to be relatively homogenous within the melt pools, but higher concentrations of Al are observed in Mn and Si deficient regions at the melt pool boundaries. During melting, these boundaries solidify starting from zero velocity and have lower solidification growth rates compared to the rest of the melt pool. This allows for increased segregation of solute elements at the melt pool boundaries compared to the higher growth rate melt pool centers [34].

Fig. 6d displays microcracking and microcavitation occurring along cellular sub-grain boundaries, which is indicative of solidification cracking (also known as hot-cracking). As discussed in Section 1, Al additions to Fe–Mn–Al–C alloys make them more susceptible to solidification cracking due to the increased solidification range [21]. However, Figs. 4 and 5 demonstrate that selection of process parameters can help mitigate solidification cracking in Fe–30Mn–9Al–1Si-0.5Mo-0.9C. Specimens printed with a scan rotation of 67° were observed to contain slightly more cracks compared to those printed at 90°. Almost twice as many microcracks were observed in cube 6 compared to the other

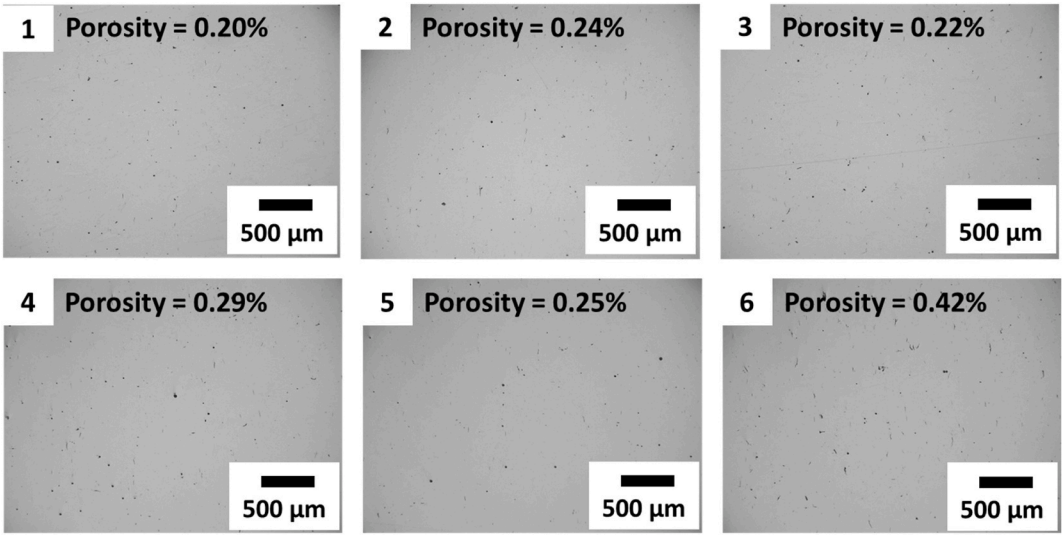

Fig. 4. Optical micrographs of polished L-PBF fabricated cube cross sections for the cubes listed in Table 1. The viewing plane is normal to the build direction in all the micrographs displayed. Porosity values calculated using thresholding image analysis are reported in each micrograph.

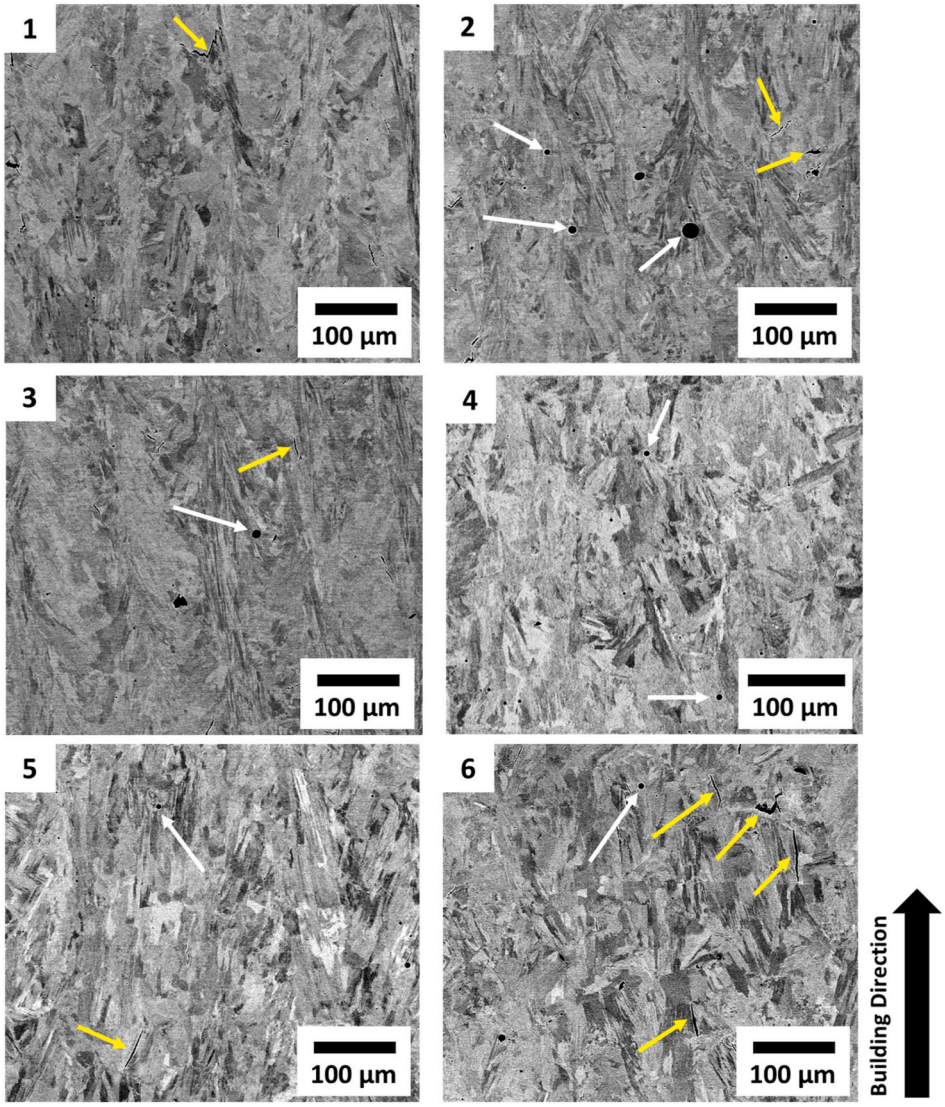

Fig. 5. Low magnification backscattered electron micrographs of the polished L-PBF fabricated cube cross sections listed in Table 1. Examples of spherical porosity observed in the micrographs are identified by the white arrows, while examples of microcracking are identified by yellow arrows. The viewing plane is normal to the build direction in all the micrographs displayed. (For interpretation of the references to colour in this figure legend, the reader is referred to the Web version of this article.)

specimens printed in this study. It is not clear why cube 6 specifically contained more cracks compared to the other specimens, especially considering the volumetric energy densities used for all the cubes are about the same. However, these results indicate that it may be possible to fully mitigate cracking with parameters not explored here such as substrate preheating.

Low magnification WDS maps displayed in Fig. 8 reveal macro-inhomogeneity in Mn, while Al, Si, and Mo are relatively homogenous. Macro-inhomogeneity in Mn and Al were also reported by Köhnen et al. [17] for Fe–21Mn–5Al-0.3C, though a thorough discussion was not provided. Macro-segregation is not commonly observed in L-PBF. Additionally, the observed Mn macro-segregation appears to be contained within melt pool structures. This phenomenon is likely the result of compositional inhomogeneities in the powder which results in convective mixing of Mn within each melt pool as the laser melts powder particles with varying Mn composition together. Although only cube 1 is presented in Fig. 8, similar macro-inhomogeneity of Mn was observed in all the cubes fabricated in this study.

Phase analysis and macro-texture determined via X-ray diffraction (XRD) are illustrated in Fig. 9. Diffraction peaks are observed at 42.44°, 49.45°, and 72.43° which correspond to (111), (200), and (220) γ austenite respectively. Austenite was the only observable phase in the XRD data for all specimens. A strong (111) macro-texture is observed in specimens printed with a 90° scan rotation (cubes 1–3). In contrast, specimens printed with a 67° scan rotation are observed to have larger (200) diffraction peaks along with the dominant (111) texture. The effect of scan rotation on reducing texture in austenitic alloys has been reported in the literature [49,50]. Scan rotations that capture a variety of different scan angles during a build, such as a 67° scan rotation, promote misalignment between the thermal gradient generated by the laser and the growth direction of columnar grains in previous layers. In the case of the 90° scan rotation, only two laser path directions are effectively captured, and the scan is exactly repeated every four layers. This results in a higher degree of alignment between columnar grains in previous layers and the thermal gradient, allowing grains to conserve their crystallographic alignment as well as the energy required for grain nucleation.

Meso-texture and crystallographic data collected by electron backscattered diffraction (EBSD) are displayed in Fig. 10 as inverse pole figure (IPF) maps and pole figures (PF). Average grain size and aspect ratio data corresponding to these results are listed in Table 3. Columnar austenitic grains oriented in the build direction are observed in all the cubes. Although all the specimens have average grain sizes within one standard deviation of each other, cubes 3 & 6 both appear to have the smallest average grain size (33 µm), and both cubes were printed with highest linear energy density parameter set (150 W, 0.8 m/s, 105 µm) used in this study. Average grain sizes in cubes 1 & 4 (printed at 90 W, 0.55 m/s, 90 µm) also appear to be very similar with only a 1.4 µm

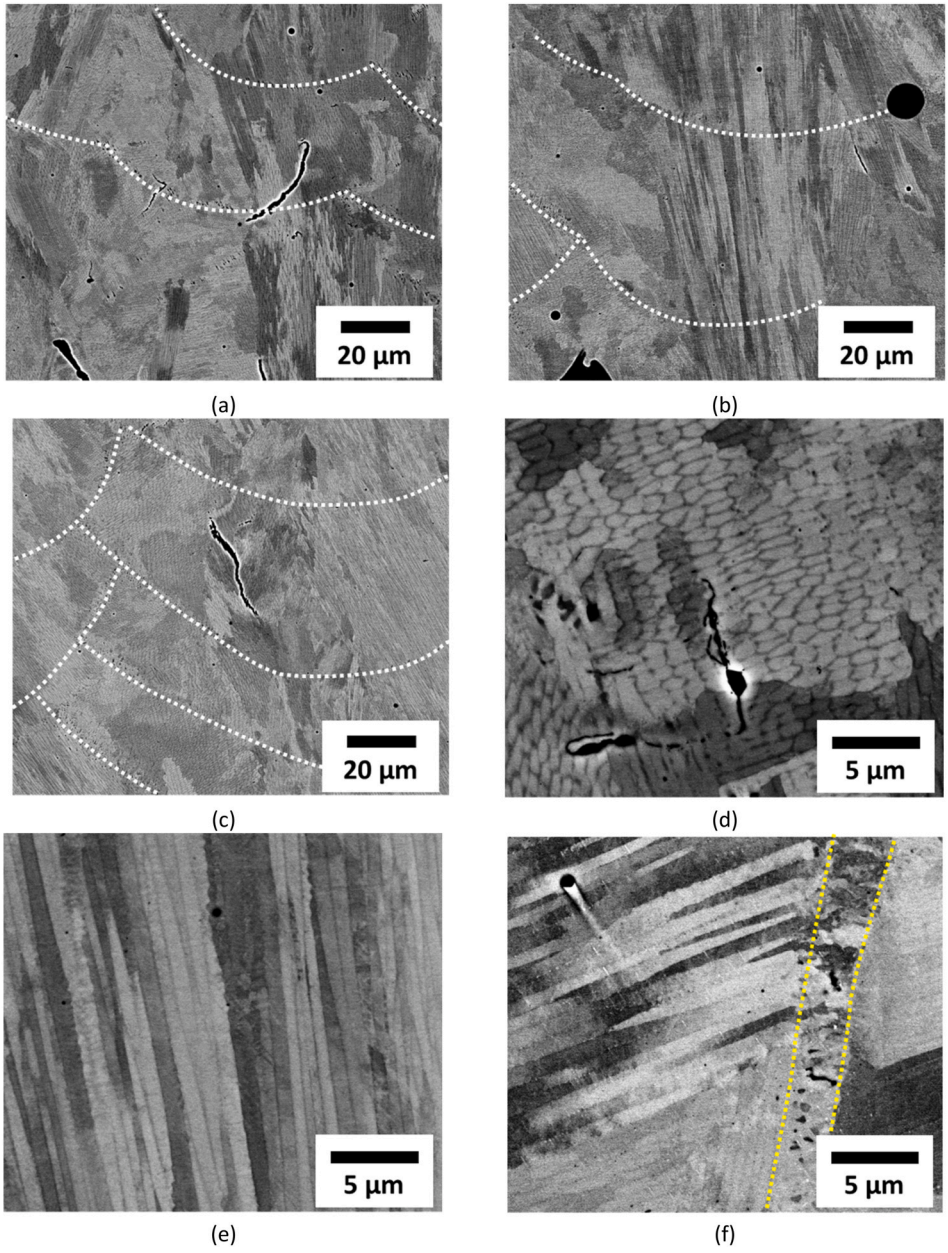

Fig. 6. High magnification backscattered electron micrographs of polished L-PBF fabricated cube cross sections. a) A micrograph of cube 2, b) and c) micrographs of cube 3 showing melt pools, microcracks, spherical pores and epitaxial grains. White dotted lines indicate melt pool boundaries. High magnification micrographs of d) cube 2 showing cellular dendritic sub-grain structures and small microcracks along the sub-grain boundaries, e) cube 3 showing columnar dendritic sub-grain structures, and f) cube 4 showing columnar dendritic sub-grain structures and a melt pool boundary zone containing smaller equiaxed sub-grain features. The melt pool boundary zone is indicated between the yellow dotted lines. The viewing plane is normal to the build direction in all the micrographs displayed. (For interpretation of the references to colour in this figure legend, the reader is referred to the Web version of this article.)

difference and an average value of ~45 µm. Cubes 2 & 5 are printed at the lowest linear energy density parameter set in this study (120 W, 0.8 m/s, 85 µm) and are measured to have average grain sizes of 53 µm and 37 µm respectively, displaying more variation compared to the other specimens. However, cube 2 had the lowest aspect ratio grains out of the specimens printed at 90° scan rotation, indicating thinner columnar grain structures compared to the other specimens. Cube 5 also showed the lowest aspect ratio grains out of the specimens printed at 67° scan rotation. IPF maps and PFs indicate that all specimens are weakly textured, and no dominant orientation is observed.

3.3. Mechanical properties

Quasi-static tensile tests carried out at room temperature were conducted on Fe–30Mn–9Al–1Si-0.5Mo-0.9C. The resulting stress strain curves are displayed in Fig. 11, and tabulated mechanical property data is presented in Table 3. Tensile specimens printed at parameter sets 1–6 listed in Table 1 were tested with two different orientations with respect to the building direction. In these tests, the loading axis was oriented both perpendicular and parallel to the build direction. Significant anisotropy is observed in mechanical properties for all specimens. Specimens tested perpendicular to the building direction had an average yield strength (YS) 25 MPa greater than those tested in the building direction. Both ultimate tensile strength (UTS) and ductility were observed to be greater in the building direction. The largest UTS observed in the building direction reached up to 1292 MPa in specimen 1, compared to 1133 MPa perpendicular to the building direction in specimen 5. This discrepancy in UTS occurs due to the drop in ductility observed from loading specimens perpendicular to the build direction. Since Fe–30Mn–9Al–1Si-0.5Mo-0.9C displays significant work hardening characteristics, early fracture in the perpendicularly oriented specimens also results in lower strength. Specimen 5 had the largest elongation to fracture observed in both orientations, with fracture occurring at 35.8% in the build direction and 19.7% perpendicular to the build direction.

Variations in mechanical properties between parameter sets appears

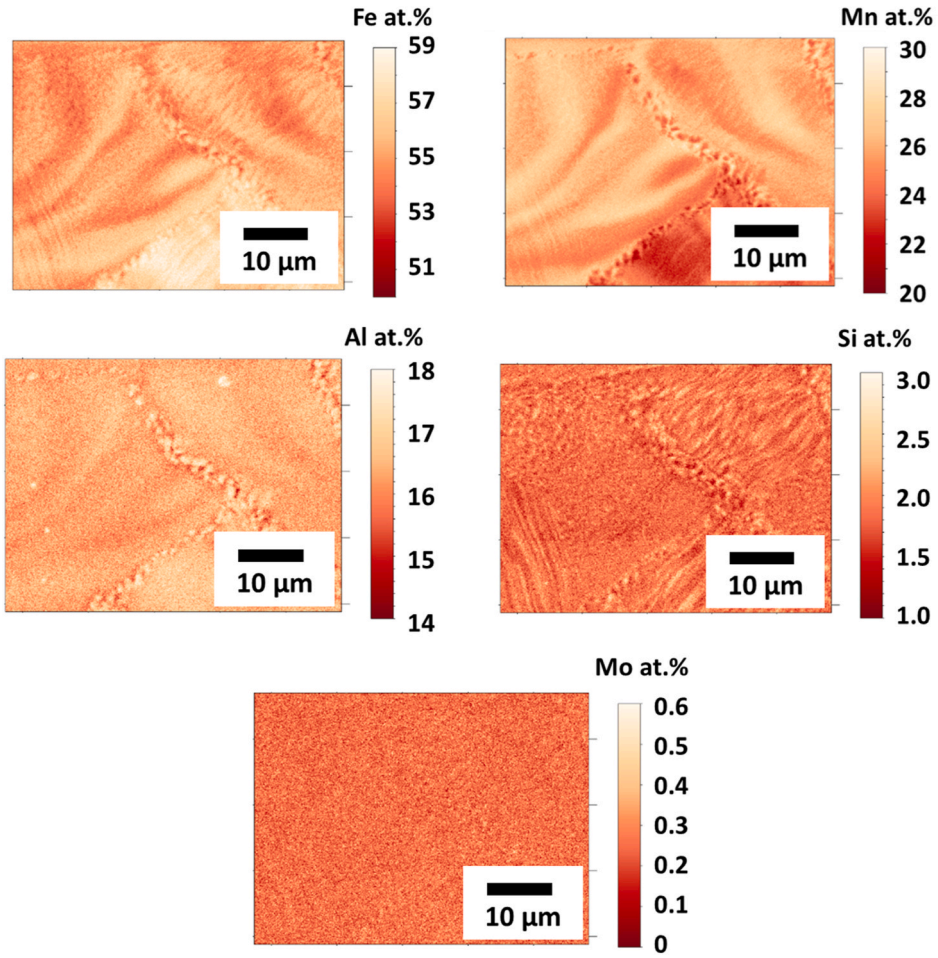

Fig. 7. High magnification WDS maps of cube 1. Quantitative elemental compositions are displayed in at.% for Fe, Mn, Al, Si, and Mo. The viewing plane is normal to the build direction in each WDS map.

to be influenced by the differences in microcracking levels reported in Fig. 4, especially perpendicular to the build direction. Cube 1 was observed to contain the lowest amount of microcracking out of the specimens printed with a 90° scan rotation (cubes 1–3) and displays superior ductility perpendicular to the build direction compared to cubes 2 & 3. Similarly, cube 5 displays the highest ductility in both directions, and was measured to contain the lowest microcracking values out of the specimens printed with a 67° scan rotation (cubes 4–6). Since microcracking is observed to be chiefly oriented in the build direction, stress concentration at the crack tips increases significantly when loaded perpendicular to this direction. This results in both substantial anisotropy in ductility, as well as the observed mechanical property differences between specimens depending on the microcrack content. Even with the existence of microcracks within the material, Fe–30Mn–9Al–1Si-0.5Mo-0.9C achieved nearly 1300 MPa UTS with ~36% ductility in the build direction and 1130 MPa UTS at ~20% ductility perpendicular to the build direction in the as-printed condition. The authors speculate that significant improvement in anisotropy can be achieved if microcracking can be fully mitigated in this alloy. This is a topic of ongoing investigation.

Picak et al. [35] reported significant anisotropy in the mechanical properties of hot rolled, annealed, and aged (forming κ-carbides) Fe–30Mn–9Al–1Si-0.5Mo-0.9C, as can be seen in Fig. 11. This anisotropy was attributed to large anisotropic lamellar segregation structures of manganese resulting in delamination-induced cleavage fracture perpendicular to the lamellae. The as-printed material reported here achieved 200 MPa lower strength in the building direction as compared to the conventionally processed material tested in the transverse direction. However, similar or improved ductility was observed in the as-printed specimens compared to the conventionally processed samples in Ref. [35]. Approximately 3% larger elongation to fracture was observed in the building direction compared to conventionally processed materials tested in the transverse direction, and 15% larger elongation to fracture and 350 MPa greater tensile strength was observed perpendicular to the building direction as compared to conventionally processed materials in the normal direction (perpendicular to the lamellae). This demonstrates that as-printed specimens show improved tensile isotropy as compared to conventionally processed Fe–30Mn–9Al–1Si-0.5Mo-0.9C. These differences are likely due to the refinement of Mn segregation structures in as-printed specimens, as compared to the macro-scale laminated Mn segregation that occurs in the wrought material and remains after thermal processing. Macroscopic chemical inhomogeneities in the wrought material were observed to result in inhomogeneous formation of κ-carbide precipitates which exacerbated delamination that occurred at the interfaces between Mn-rich and Mn-depleted regions of the material [35]. However, the chemical inhomogeneities were still observed to lead to significant anisotropy in the wrought material even after κ-carbides were dissolved with solution heat treatments [35]. In contrast, the Mn segregation that occurs in melt pool structures in as-printed specimens (Fig. 8) is not oriented in a particular direction. The scale of as-printed micro-segregation is significantly lower in the as-printed material as these structures are contained within each individual melt pool which are <100 µm wide in comparison to the laminated wrought material

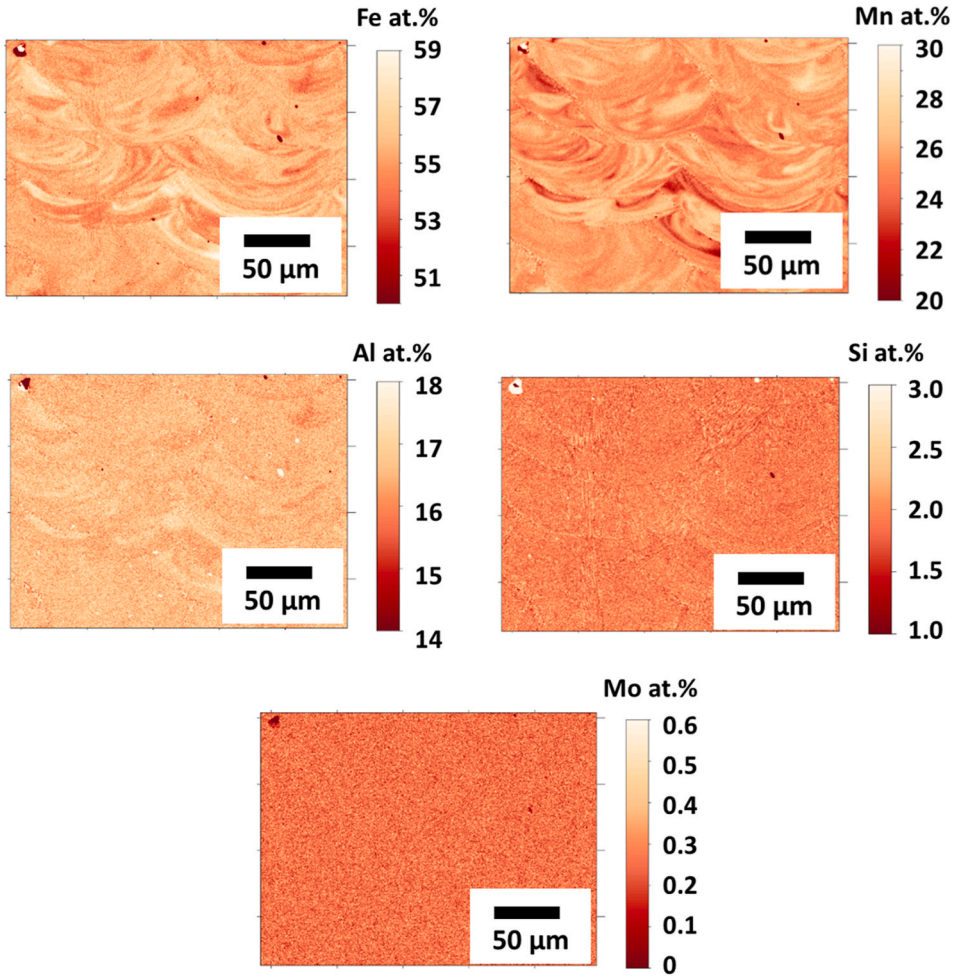

Fig. 8. Low magnification WDS maps of Cube 1. Quantitative elemental compositions are displayed in at.% for Fe, Mn, Al, Si, and Mo. The viewing plane is normal to the build direction in each WDS map.

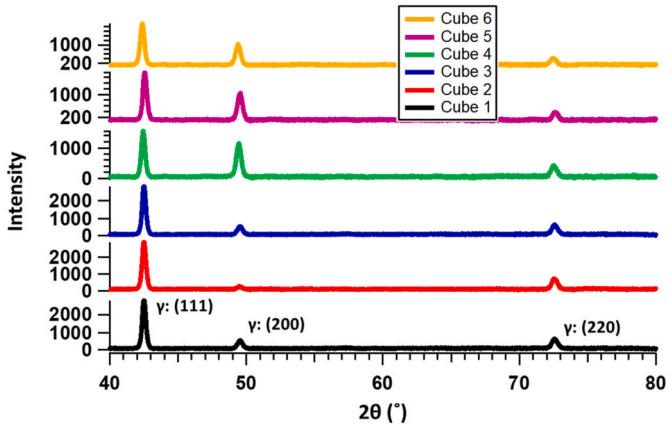

Fig. 9. X-ray diffraction (XRD) spectra in cubes 1–6 listed in Table 1. Diffraction peaks associated with γ austenite in the (111), (200), and (220) planes are observed in all the cubes. XRD spectra were collected in the plane normal to the build direction.

structures [35]. Additionally, Mn micro-segregation in the form of cellular-dendritic structures is concentrated chiefly at melt pool boundaries and do not appear consistently throughout the melt pools. These microstructural refinements in the L-PBF processed material led to the significant reduction in the mechanical property anisotropy compared to the wrought material, despite microcracking oriented in the build direction of as-printed specimens.

4. Summary and conclusions

The effects of L-PBF additive manufacturing on the lightweight austenitic steel Fe–30Mn–9Al–1Si-0.5Mo-0.9C are presented here. A process optimization framework was implemented to develop processing maps for this alloy, resulting in the fabrication of near fully dense specimens at a wide range of process parameters. Additionally, specimens were built with two scan rotations (90° and 67°) to determine their effects on microstructure and mechanical properties. The following conclusions can be drawn from this study.

- Near-full density Fe–30Mn–9Al–1Si-0.5Mo-0.9C parts were successfully fabricated using L-PBF. All as-printed specimens were observed to have >99% Archimedes density, the majority of which also achieved >99.7% density measured using porosity content. However, solidification microcracking was observed in all the as-fabricated samples due to the large solidification range of the material.
- Noticeable Mn and Si cellular-dendritic segregation was observed throughout the material, and more prominent segregation of these elements was detected along the melt pool boundaries. Additionally, higher concentrations of Al were observed in Mn and Si depleted regions within the melt pool boundaries. However, no secondary phases or precipitates were detected by x-ray diffraction.

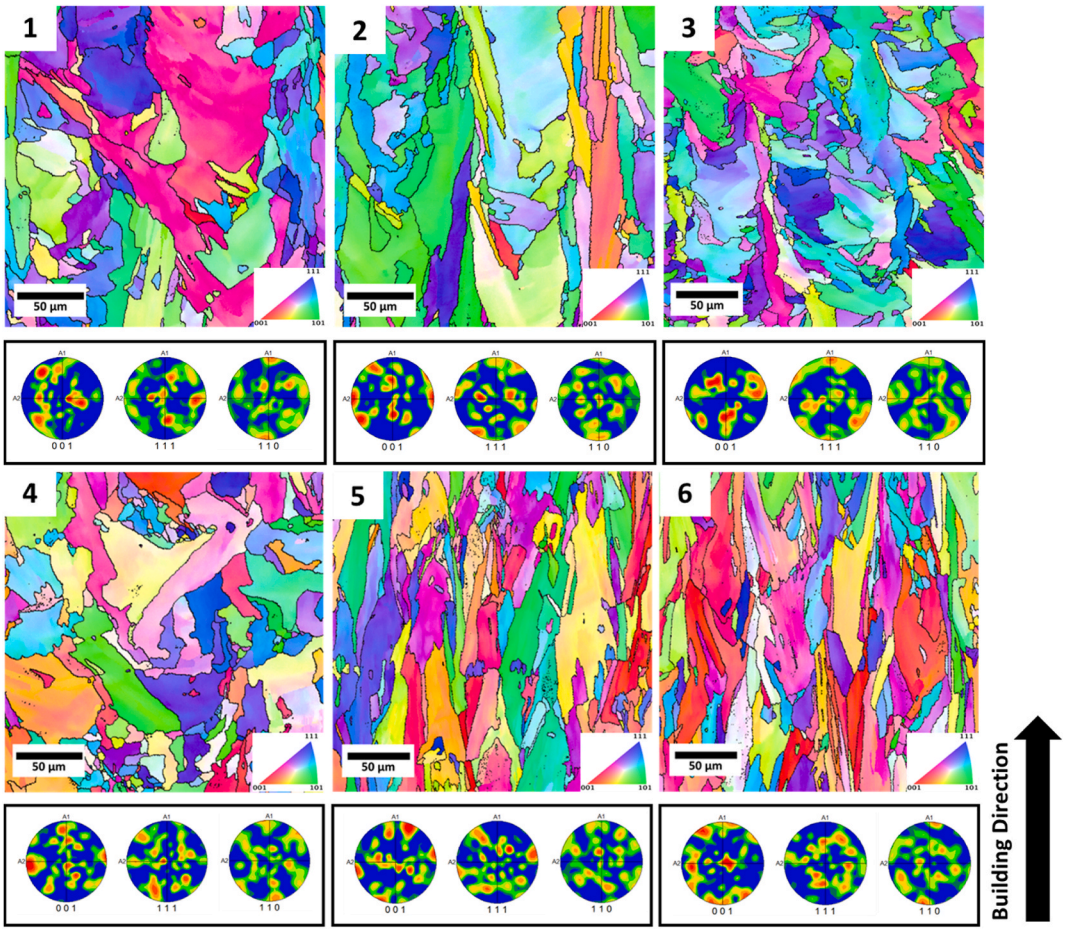

Fig. 10. Electron backscattered diffraction (EBSD) inverse pole figure (IPF) maps and pole figures (PF) collected from a viewing plane parallel to the building plane in cubes 1–6 listed in Table 1. Refer to Table 3 for corresponding average grain size and aspect ratio data corresponding to the IPF maps. All maps were indexed for face-centered-cubic (FCC) austenite. The viewing plane is normal to the build direction in each EBSD map.

Table 3
Average microstructural features and mechanical properties of Fe–30Mn–9Al–1Si-0.5Mo-0.9C in the as-fabricated condition. Average grain sizes and aspect ratios were extracted from the EBSD data. Tensile properties were measured in 3 separate tests for each parameter set and loading orientation, and the values reported in this table are averaged from these tests. The ± values represent one standard deviation from the mean for all reported data. Mechanical property values are reported for true stress-strain data.

Parameter Set	Average Grain Size (μm)	Average Grain Aspect Ratio	Orientation with Build Direction	Ultimate Tensile Strength (MPa)	Elongation (%)	Yield Strength (MPa)
1	45.4 ± 25.1	0.346 ± 0.138	Perpendicular	1123.3 ± 11.0	17.9 ± 0.8	743.3 ± 9.8
			Parallel	1291.7 ± 13.4	34.2 ± 1.5	720.4 ± 10.4
2	53.2 ± 28.8	0.231 ± 0.136	Perpendicular	1008.4 ± 99.9	14.8 ± 1.9	704.3 ± 43.7
			Parallel	1267.5 ± 15.1	35.2 ± 1.9	705.0 ± 4.2
3	33.7 ± 17.4	0.341 ± 0.129	Perpendicular	1019.8 ± 14.0	13.1 ± 0.7	736.7 ± 4.5
			Parallel	1235.0 ± 3.1	32.4 ± 0.2	699.3 ± 7.6
4	46.8 ± 24.9	0.370 ± 0.106	Perpendicular	1105.0 ± 22.1	17.7 ± 0.9	746.7 ± 13.6
			Parallel	1237.8 ± 1.9	31.2 ± 0.2	715.7 ± 8.7
5	37.1 ± 21.0	0.195 ± 0.109	Perpendicular	1133.0 ± 11.9	19.7 ± 0.9	743.3 ± 6.9
			Parallel	1282.9 ± 7.8	35.8 ± 0.1	703.0 ± 2.9
6	33.0 ± 16.3	0.205 ± 0.107	Perpendicular	1034.0 ± 47.3	15.4 ± 2.6	726.0 ± 9.9
			Parallel	1231.3 ± 6.0	30.9 ± 0.8	707.3 ± 6.1

- As-fabricated Fe–30Mn–9Al–1Si-0.5Mo-0.9C achieved an impressive 1300 MPa strength and ~36% ductility in the build direction. Substantial anisotropy was observed in the mechanical properties of the material due to microcracks oriented along the build direction. Specimens loaded perpendicular to this direction increased the stress at the crack tips, resulting in a drop in mechanical properties (1130 MPa and 20% ductility). Similar mechanical properties were observed for specimens printed with varied process parameters, with minor differences occurring due to variations in microcrack content. The best mechanical properties were observed in material fabricated at 120 W, 0.8 m/s, 85 μm hatch spacing, and a 67° scan rotation.

Credit authorship contribution statement

R.S and **I.K.** contributed to the conceptualization of the experiments and experimental methodology. **R.S** contributed to paper writing and

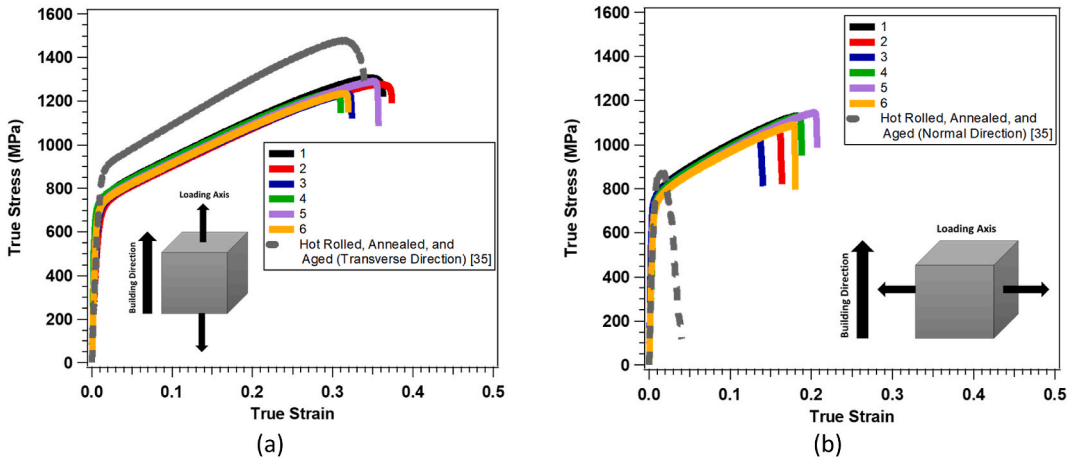

Fig. 11. True stress vs. true strain responses for cubes 1–6, a) for specimens loaded in the build direction, and b) for specimens loaded perpendicular to the build direction. Hot rolled, annealed, and aged specimens tested in the transverse (a) and normal (b) directions reported in Ref. [35] is also plotted.

revisions, post processing of the material, and conducting all characterization and mechanical testing experiments. **J.Y.** contributed to fabricating the additively manufactured material used for experiments and constructing the printability map. **A.W.** contributed to optical and electron micrograph characterization of the material, extracting measurements from characterization experiments, mechanical testing and data analysis. **S.G.**, **P.F.**, and **B.G.** contributed to experimental planning and sourcing the raw material used for experiments. **A.E., R.A., and I.K.** co-supervised the scholarly work, and secured all resources needed to conduct the work. All authors reviewed the manuscript.

Declaration of competing interest

The authors declare the following financial interests/personal relationships which may be considered as potential competing interests: Ibrahim Karaman reports financial support was provided by US Army Research Office. Ibrahim Karaman reports financial support was provided by Air Force Research Laboratory.

Data availability

Data will be made available on request.

Acknowledgements

This work was carried out with the support from the Army Research Office (ARO) under Contract No. W911NF-18-1-0278 and the U.S. Air Force Research Laboratory through the Grant number FA8651-19-1-0005. The complete draft of the manuscript was written by the first author (RS) under the auspices of the U.S. Department of Energy by Lawrence Livermore National Laboratory under Contract DE-AC52-07NA27344. Dr. Elwany acknowledges support from National Science Foundation (NSF) Award No. CMMI-1846676. The authors would like to acknowledge Dr. Andrew Mott for his support in operating the Cameca SXFive Microprobe.

References

[1] E. Liverani, S. Toschi, L. Ceschini, A. Fortunato, Effect of selective laser melting (SLM) process parameters on microstructure and mechanical properties of 316L austenitic stainless steel, J. Mater. Process. Technol. 249 (2017) 255–263.
[2] T. DebRoy, H.L. Wei, J.S. Zuback, T. Mukherjee, J.W. Elmer, J.O. Milewski, A. M. Beese, A. Wilson-Heid, A. De, W. Zhang, Additive manufacturing of metallic components–process, structure and properties, Prog. Mater. Sci. 92 (2018) 112–224.
[3] R. Seede, D. Shoukr, B. Zhang, A. Whitt, S. Gibbons, P. Flater, A. Elwany, R. Arroyave, I. Karaman, An ultra-high strength martensitic steel fabricated using selective laser melting additive manufacturing: densification, microstructure, and mechanical properties, Acta Mater. 186 (2020) 199–214.
[4] R. Seede, B. Zhang, A. Whitt, S. Picak, S. Gibbons, P. Flater, A. Elwany, R. Arroyave, I. Karaman, Effect of heat treatments on the microstructure and mechanical properties of an ultra-high strength martensitic steel fabricated via laser powder bed fusion additive manufacturing, Addit. Manuf. 47 (2021), 102255.
[5] K.N. Amato, S.M. Gaytan, L.E. Murr, E. Martinez, P.W. Shindo, J. Hernandez, S. Collins, F. Medina, Microstructures and mechanical behavior of Inconel 718 fabricated by selective laser melting, Acta Mater. 60 (2012) 2229–2239.
[6] Z. Wang, K. Guan, M. Gao, X. Li, X. Chen, X. Zeng, The microstructure and mechanical properties of deposited-IN718 by selective laser melting, J. Alloys Compd. 513 (2012) 518–523.
[7] W.M. Tucho, P. Cuvillier, A. Sjolyst-Kverneland, V. Hansen, Microstructure and hardness studies of Inconel 718 manufactured by selective laser melting before and after solution heat treatment, Mater. Sci. Eng. 689 (2017) 220–232.
[8] R. Seede, A. Mostafa, V. Brailovski, M. Jahazi, M. Medraj, Microstructural and microhardness evolution from homogenization and hot isostatic pressing on selective laser melted Inconel 718: structure, texture, and phases, J. Manuf. Mater. Process. 2 (2018) 30.
[9] K. Kempen, L. Thijs, J. Van Humbeeck, J.P. Kruth, Mechanical properties of AlSi10Mg produced by selective laser melting, Phys. Procedia (2012) 439–446.
[10] N. Read, W. Wang, K. Essa, M.M. Attallah, Selective laser melting of AlSi10Mg alloy: process optimisation and mechanical properties development, Mater. Des. 65 (2015) 417–424.
[11] D. Agius, K. Kourousis, C. Wallbrink, A review of the as-built SLM Ti-6Al-4V mechanical properties towards achieving fatigue resistant designs, Metals 8 (2018) 75.
[12] Y. Wang, C. Kamath, T. Voisin, Z. Li, A processing diagram for high-density Ti-6Al-4V by selective laser melting, Rapid Prototyp. J. 24 (2018) 1469–1478.
[13] H. Zhang, H. Zhu, T. Qi, Z. Hu, X. Zeng, Selective laser melting of high strength Al-Cu-Mg alloys: processing, microstructure and mechanical properties, Mater. Sci. Eng. 656 (2016) 47–54.
[14] W. Xiong, L. Hao, Y. Li, D. Tang, Q. Cui, Z. Feng, C. Yan, Effect of selective laser melting parameters on morphology, microstructure, densification and mechanical properties of supersaturated silver alloy, Mater. Des. 170 (2019), 107697.
[15] A. Iveković, N. Omidvari, B. Vrancken, K. Lietaert, L. Thijs, K. Vanmeensel, J. Vleugels, J.P. Kruth, Selective laser melting of tungsten and tungsten alloys, Int. J. Refract. Met. Hard Mater. 72 (2018) 27–32.
[16] K. Karayagiz, L. Johnson, R. Seede, V. Attari, B. Zhang, X. Huang, S. Ghosh, T. Duong, I. Karaman, A. Elwany, R. Arroyave, Finite interface Dissipation phase Field modeling of Ni-Nb under additive manufacturing conditions, Acta Mater. 185 (2020) 320–339.
[17] P. Köhnen, S. Ewald, J.H. Schleifenbaum, A. Belyakov, C. Haase, Controlling microstructure and mechanical properties of additively manufactured high-strength steels by tailored solidification, Addit. Manuf. 35 (2020), 101389.
[18] F. Kies, P. Köhnen, M.B. Wilms, F. Brasche, K.G. Pradeep, A. Schwedt, S. Richter, A. Weisheit, J.H. Schleifenbaum, C. Haase, Design of high-manganese steels for additive manufacturing applications with energy-absorption functionality, Mater. Des. 160 (2018) 1250–1264.
[19] W. Li, J. Li, X. Duan, C. He, Q. Wei, Y. Shi, Dislocation-induced ultra-high strength in a novel steel fabricated using laser powder-bed-fusion, Mater. Sci. Eng. 832 (2022), 142502.
[20] S.A.H. Motaman, C. Haase, The microstructural effects on the mechanical response of polycrystals: a comparative experimental-numerical study on conventionally and additively manufactured metallic materials, Int. J. Plast. 140 (2021), 102941.
[21] S. Chen, R. Rana, A. Haldar, R.K. Ray, Current state of Fe-Mn-Al-C low density steels, Prog. Mater. Sci. 89 (2017) 345–391.
[22] H. Kim, D.-W. Suh, N.J. Kim, Fe–Al–Mn–C lightweight structural alloys: a review on the microstructures and mechanical properties, Cience Technol. Adv. Mater. 14 (2013), 14205.

[23] K. Choi, C.H. Seo, H. Lee, S.K. Kim, J.H. Kwak, K.G. Chin, K.T. Park, N.J. Kim, Effect of aging on the microstructure and deformation behavior of austenite base lightweight Fe–28Mn–9Al–0.8 C steel, Scripta Mater. 63 (2010) 1028–1031.
[24] J.B. Seol, A brief review of κ-carbide in Fe-Mn-Al-C model alloys, Appl. Microsc. 48 (2018) 117–121.
[25] P. Chen, X. Li, H. Yi, The κ-carbides in low-density Fe-Mn-Al-C steels: a review on their structure, precipitation and deformation mechanism, Metals 10 (2020) 1021.
[26] J. Lee, H. Kim, K. Jeong, S.J. Park, J. Moon, S.G. Kang, H.N. Han, Prediction of precipitation kinetics and strengthening in FeMnAlC lightweight steels, J. Mater. Res. Technol. 14 (2021) 2897–2908.
[27] L. Bartlett, D. Van Aken, High manganese and aluminum steels for the military and transportation industry, JOM 66 (2014) 1770–1784.
[28] N. Kouraytem, P.J. Chiang, R. Jiang, C. Kantzos, J. Pauza, R. Cunningham, Z. Wu, G. Tang, N. Parab, C. Zhao, K. Fezzaa, Solidification crack propagation and morphology dependence on processing parameters in AA6061 from ultra-high-speed x-ray visualization, Addit. Manuf. 42 (2021), 101959.
[29] W. Stopyra, K. Gruber, I. Smolina, T. Kurzynowski, B. Kuźnicka, Laser powder bed fusion of AA7075 alloy: influence of process parameters on porosity and hot cracking, Addit. Manuf. 35 (2020), 101270.
[30] B. Zhang, R. Seede, L. Xue, K.C. Atli, C. Zhang, A. Whitt, I. Karaman, R. Arroyave, A. Elwany, An efficient framework for printability assessment in laser powder bed fusion metal additive manufacturing, Addit. Manuf. (2021), 102018.
[31] A. Pfaff, M. Jäcklein, M. Schlager, W. Harwick, K. Hoschke, F. Balle, An empirical approach for the development of process parameters for laser powder bed fusion, Materials 13 (2020) 5400.
[32] J.N. Zhu, E. Borisov, X. Liang, E. Farber, V.A. Hermans, M.J.M. Popovich, Predictive analytical modelling and experimental validation of processing maps in additive manufacturing of nitinol alloys, Addit. Manuf. 38 (2021), 101802.
[33] L. Xue, K.C. Atli, S. Picak, C. Zhang, B. Zhang, A. Elwany, R. Arroyave, I. Karaman, Controlling martensitic transformation characteristics in defect-free NiTi shape memory alloys fabricated using laser powder bed fusion and a process optimization framework, Acta Mater. (2021), 117017.
[34] R. Seede, J. Ye, A. Whitt, W. Trehern, A. Elwany, R. Arroyave, I. Karaman, Effect of composition and phase diagram features on printability and microstructure in laser powder bed fusion: development and comparison of processing maps across alloy systems, Addit. Manuf. 47 (2021), 102258.
[35] S. Picak, M.W. Vaughan, O. El Atwani, A. Mott, K.R. Limmer, I. Karaman, Effects of chemical segregation on ductility-anisotropy in high strength Fe-Mn-Al-C lightweight austenitic steels, Acta Mater. 245 (2023), 118589.
[36] T.W. Eagar, N.-S. Tsai, Temperature fields produced by traveling distributed heat sources, Weld. J. 62 (1983) 346–355.
[37] L. Johnson, M. Mahmoudi, B. Zhang, R. Seede, J.T. Maier, H.J. Maier, I. Karaman, A. Elwany, Assessing printability maps in additive manufacturing of metal alloys, Acta Mater. 176 (2019) 199–210.
[38] H. Gong, H. Gu, K. Zeng, J. Dilip, D. Pal, B. Stucker, J.J. Lewandowski, Melt pool characterization for selective laser melting of Ti-6Al-4V pre-alloyed powder, solid free, Fabr. Symp. (2014).
[39] R. Rai, J.W. Elmer, T.A. Palmer, T. Debroy, Heat transfer and fluid flow during keyhole mode laser welding of tantalum, Ti-6Al-4V, 304L stainless steel and vanadium, J. Phys. D Appl. Phys. 40 (2007) 5753–5766.
[40] M.C. Kennedy, A. O'Hagan, Bayesian calibration of computer models, J. R. Stat. Soc. Ser. B (Statistical Methodol. 63 (2001) 425–464.
[41] J.D. Roehling, A. Perron, J.L. Fattebert, T. Haxhimali, G. Guss, T.T. Li, D. Bober, A. W. Stokes, A.J. Clarke, P.E.A. Turchi, M.J. Matthews, J.T. McKeown, Rapid solidification in bulk Ti-Nb alloys by single-track laser melting, JOM 70 (2018) 1589–1597.
[42] M. Letenneur, A. Kreitcberg, V. Brailovski, Optimization of laser powder bed fusion processing using a combination of melt pool modeling and Design of experiment approaches: density control, J. Manuf. Mater. Process. 3 (2019) 21.
[43] M. Letenneur, V. Brailovski, A. Kreitcberg, V. Paserin, I. Bailon-Poujol, Laser powder bed fusion of water-atomized iron-based powders: process optimization, J. Manuf. Mater. Process. 1 (2017) 23.
[44] B. Scholkopf, A.J. Smola, Learning with Kernels: Support Vector Machines, Regularization, MIT Press, 2001.
[45] J.A.K. Suykens, J. Vandewalle, Least squares support vector machine classifiers, Neural Process. Lett. 9 (1999) 293–300.
[46] W. Rasband, ImageJ, U. S. Natl. Institutes Heal, Bethesda, Maryland, USA, 2012. //imagej.nih.gov/ij/).
[47] M. Daamen, C. Haase, J. Dierdorf, D.A. Molodov, G. Hirt, Twin-roll strip casting: a competitive alternative for the production of high manganese steels with advanced mechanical properties, Mater. Sci. Eng. 627 (2015) 72–81.
[48] M. Daamen, B. Wietbrock, S. Richter, G. Hirt, Strip casting of a high manganese steel (FeMn22C0.6) compared with a process chain consisting of ingot casting and hot forming steel, Steel Res. Int. 82 (2011) 70–75.
[49] J.J. Marattukalam, D. Karlsson, V. Pacheco, P. Beran, U. Wiklund, U. Jansson, B. Hjörvarsson, M. Sahlberg, The effect of laser scanning strategies on texture, mechanical properties, and site-specific grain orientation in selective laser melted 316L SS, Mater. Des. 193 (2020), 108852.
[50] M.S. Pham, B. Dovgyy, P.A. Hooper, C.M. Gourlay, A. Piglione, The role of side-branching in microstructure development in laser powder-bed fusion, Nat. Commun. 11 (2020) 1–12.